Preprints (www.preprints.org) | NOT PEER-REVIEWED | Posted: 29 April 2022 doi:10.20944/preprints202204.0294.v1

Article

Design and Optimization of GeSn Waveguide Photodetectors for 2-μm Band Silicon Photonics

Soumava Ghosh[1], Radhika Bansal[2], Greg Sun[3], Richard A. Soref[3], Hung-Hsiang Cheng[4], and Guo-En Chang[2,*]

[1] Institute of Radio Physics and Electronics, University of Calcutta, Kolkata 700009, India; ghosh-soumava2@gmail.com (S.G.)
[2] Department of Mechanical Engineering, and Advanced Institute of Manufacturing with High-Tech Innovations (AIM-HI), National Chung Cheng University, Chiyai County 62102, Taiwan; d09420005@ccu.edu.tw (R.B.)
[3] Department of Engineering, University of Massachusetts–Boston, Boston, Massachusetts 02125, USA; greg.sun@umb.edu (G.S.); richard.soref@umb.edu (R.S.)
[4] Center for Condensed Matter Sciences and Graduate Institute of Electronics Engineering, National Taiwan University, Taipei 106, Taiwan; hhcheng@ntu.edu.tw (H.-H.C.)

* Correspondence: imegec@ccu.edu.tw; Tel.: +886-5-2720411 (ext. 33324)

Abstract: Silicon photonics is emerging as a competitive platform for electronic-photonic integrated circuits (EPICs) at the 2 μm wavelength band where GeSn photodetectors (PDs) have proven to be efficient PDs. Here, we present a comprehensive theoretical study of GeSn vertical *p-i-n* homojunction waveguide photodetectors (WGPDs) that have a strain-free and defect-free GeSn active layer for 2-μm Si-based EPICs. The use of a narrow-gap GeSn alloy as the active layer can fully cover entire the 2 μm wavelength band. The waveguide structure allows for decoupling the photon-absorbing path and the carrier-collection path, thereby allowing for simultaneous achievement of high-responsivity and high-bandwidth (BW) operation at the 2-μm wavelength band. We present the theoretical models to calculate the carrier saturation velocities, optical absorption coefficient, responsivity, 3-dB bandwidth, zero-bias resistance, and detectivity, and optimize this device structure to achieve highest performance at the 2-μm wavelength band. The results indicate that the performance of the GeSn WGPD has strong dependence on the Sn composition and geometric parameters. The optimally designed GeSn WGPD with 10% Sn concentration can give responsivity of 1.55 A/W, detectivity of 6.12×10^{10} cmHz$^{1/2}$W^{-1} at 2 μm wavelength, and ~97 GHz BW. Therefore, this optimally designed GeSn WGPD is a potential candidate for silicon photonic EPICs offering high-speed optical communications.

Keywords: Waveguide Photodetector, Saturation velocity, R_0A parameter, Responsivity, Bandwidth, Detectivity, Silicon Photonics

1. Introduction

Fiber-optic communication systems offer strong competition to the electronic counterparts due to their low interference, low attenuation (~0.2 dB/km) and high operational speed. Although 1.31 μm and 1.55 μm wavelength bands are very popular in the telecommunication industry, the exponential growth of internet traffic has driven their data-transport capacity to the verge of its theoretical limit [1]. In addition, their bandwidths (BWs) can no longer be significantly increased using the existing technologies. Therefore, researchers are trying to develop new technologies to circumvent this bottleneck condition. A significant approach to overcome this aforesaid shortcoming is to use hollow-core photonic bandgap fibers (HC-PBGFs), which provide low loss (~0.1 dB/km)

© 2022 by the author(s). Distributed under a Creative Commons CC BY license.

with high speed ~0.98 times of *c* (velocity of light in free space) in the 2-μm wavelength band, i.e. the wavelength range of 1.8-2.1 μm [2]. Moreover, high-BW thulium-doped fiber amplifier (TDFA) light source that can emit light in the range of 1.8-2 μm is suitable for the 2-μm wavelength band [3]. Those distinctive advantages have made the 2 μm wavelength band a supplement to the 1.31 and 1.55-μm wavelength bands for next-generation high-speed fiber-optic communication. Apart from telecommunication applications, this 2-μm band can also be used in sensing and biomedical applications [4].

Photodetectors (PDs) are an essential photonic device to convert optical signals to electrical signals. For 2-μm wavelength applications, although market-dominated III-V-based short-wave infrared (SWIR) PDs show promising performance at 2-μm wavelength [5,6], their incompatibility with Si-based complementary metal-oxide-semiconductor (CMOS) processing technology has made them expensive and less possible for large-scale integration. On the other hand, over the last few decades, group-IV based SWIR PDs have attracted attention due to their compatibility with standard Si-based CMOS processing technology and their monolithically integrability on the same Si chip [7,8] to realize electronic-photonic integrated circuits (EPICs). However, Si and Ge-based SWIR PDs are not suitable for 2 μm due to their short cut-off wavelengths of 1.1 μm and 1.5 μm respectively [8,9].

There is a dramatic improvement of this situation in the last two decades, with the successful growth of a new group-IV material system, $Ge_{1-x}Sn_x$ alloys, using a suitable buffer layer on Si substrates either by molecular beam epitaxy (MBE) [10] or by chemical vapor deposition (CVD) techniques [11,12]. Adding Sn into Ge can significantly reduce the direct bandgap, thereby red-shifting the direct bandgap and thus enabling efficient photodetection in the infrared region. In addition, the standard Si-based CMOS compatibility, bandgap tunability due to Sn incorporation, direct bandgap for $x \geq 0.06$ [13], large absorption coefficient in the infrared region [14] and high carrier mobility [15] make $Ge_{1-x}Sn_x$ alloys attractive as active materials for different types of PDs [14,16-25]. A variety of normal-incidence $Ge_{1-x}Sn_x$ based *p-i-n* PDs have been demonstrated by a few groups, showing promising performance in the SWIR region, and even up to 3.7 μm [26-32]. Recent theoretical study has predicted that normal-incidence GeSn PDs' performance can be comparable to, and even better than conventional SWIR and MIR PDs [13]. However, for EPICs, planar waveguide PDs (WGPDs) are preferred for more convenient integration with other photonic devices. In addition, planar WGPDs have many unique advantages over normal-incidence PDs. First, the decoupling of the photon absorption path and the photo-generated carriers collection path in WGPDs removes the trade-off between spectral responsivity and 3-dB bandwidth (BW). Second, the long photon-absorbing path can sufficiently absorb the incident photons, thus significantly increasing the optical responsivity. This salient feature makes the WGPDs very effective for modern high-speed communication applications. Until now, only few attempts have been made to fabricate WGPDs based on bulk GeSn alloys and multiple-quantum-well (MQW) structures [33-36]. Among those studies, researchers have primarily focused on the measurement of responsivity, dark and photocurrent, and 3-dB BW of the WGPDs [33-36], showing performance superior to that of normal-incidence GeSn PDs. However, the performance

Preprints (www.preprints.org) | NOT PEER-REVIEWED | Posted: 29 April 2022 doi:10.20944/preprints202204.0294.v1

of GeSn PDs is also highly dependent on the device geometry. It is therefore important to also optimize their geometry to predict achievable performance for practical applications at the 2-μm wavelength band.

In this paper, we propose and analyze a novel GeSn homojunction vertical *p-i-n* WGPD on Si substrate to obtain simultaneously high-BW and high responsivity at the 2-μm wavelength band currently considered as a promising communications window. First, we show our proposed design of GeSn WGPDs. Then, we present analytical models to calculate the saturation velocity of carriers in GeSn, the 3-dB BW, optical responsivity and the R_0A parameters of the proposed GeSn WGPDs. Following that, we analyze the dependence of Sn content and structural parameters on the device performance and optimize the structural parameters of the proposed GeSn WGPDs to simultaneously achieve high-BW and high responsivity at 2 μm. Finally, we evaluate the detectivity of the optimally designed GeSn WGPDs and compare them with conventional SWIR and MIR PDs. These results provide useful guidelines for design high-performance GeSn WGPDs for silicon photonics operating at 2 μm wavelength band.

The rest of the paper is organized as follows, the structural architecture of the proposed WGPD is shown in Sec. 2; the theoretical models are summarized in Sec. 3; the performance analysis of the GeSn WGPD at 2 μm is discussed in Sec. 4; followed by the conclusion in Sec. 5.

2. Design of GeSn WGPDs

2.1. Design of GeSn p-i-n waveguide photodetectors

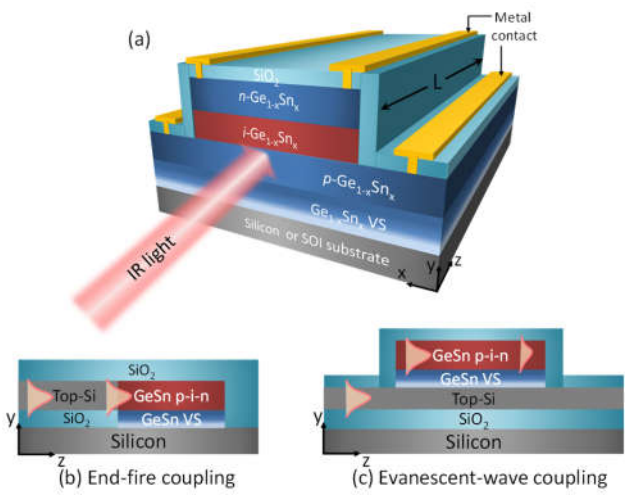

Figure 1. (**a**) Schematic diagram of our proposed homojunction GeSn vertical *p-i-n* WGPD on Si or SOI substrate. Schematics of (**b**) end-fire and (**c**) evanescent-wave coupling for the proposed GeSn WGPDs.

The structure we propose for the GeSn vertical *p-i-n* homojunction WGPD is depicted in Fig. 1. The intrinsic $Ge_{1-x}Sn_x$ absorption region is sandwiched between two heavily doped *p*- and *n*-type $Ge_{1-x}Sn_x$ layers with a doping concentration of 1×10^{19} cm^{-3}. The entire vertical *p-i-n* structure is grown on Si (001) or silicon-on-insulator (SOI) substrates via a compositionally step-graded, fully strain-relaxed $Ge_{1-x}Sn_x$ virtual substrate (VS) [13], whose thickness is set to 1000 nm, resulting in a lattice-matched strain-free GeSn *p-i-n*

homojunction structure. In addition, to predict the highest performance, the GeSn *p-i-n* structure is assumed to be defect-free [13] and the waveguide coupling efficiency to be 100%. The thickness of the *p*-type $Ge_{1-x}Sn_x$, *i*-$Ge_{1-x}Sn_x$ active layer, and *n*- $Ge_{1-x}Sn_x$ layers are t_p, t_i and t_n, respectively. Here we set t_p = 500 nm and t_n = 100 nm. The WGPD has a ridge structure down to the top surface of *p*-$Ge_{1-x}Sn_x$, and is covered by a SiO_2 layer as the electrical isolator for the $Ge_{1-x}Sn_x$ homojunction and as the cladding layer for the waveguide. The width of the ridge structure (w) is set to 1 μm for single-mode operation, while the length of photon absorption region L and the thickness of the photo-generated carriers' collection path t_i will be optimized to achieve the highest performance. Under illumination, the electron hole pairs (EHPs) generated in the $Ge_{1-x}Sn_x$ region are swept to the *n*-$Ge_{1-x}Sn_x$ and *p*-$Ge_{1-x}Sn_x$ regions due to the built-in electric field, thereby producing photocurrents.

2.2. PD to Waveguide Coupling

Several assumptions are made in this paper regarding the PD that is detailed here: (1) the PD, or a group of PDs, is part of a waveguided photonic-integrated-circuit (PIC) that is fabricated on a wafer substrate, (2) that wafer is most likely a SOI wafer, although it could alternatively be bulk silicon, (3) the PIC and typically some transistor-electronic integrated circuits are co-integrated on the SOI wafer by manufacturing in a Si CMOS foundry. Regarding the efficient optical coupling between the PD and a low-loss strip waveguide, there are several practical scenarios that are envisioned here. These feasible approaches are: (1) the undoped strip waveguide is comprised either of Si or Ge, but Si is preferred, (2) an SOI strip waveguide is end-fire coupled into the i-GeSn PD core without an air gap between the Si core and PD core because selective-area growth of the PD within an SOI "trench" is used to construct the PD, (3) or alternatively, the PD is built upon the top surface of the SOI strip in order to use "evanescent-wave" side coupling of light along the long axis of the Si strip.

Going into more detail, we are proposing two practical approaches that are illustrated in Fig. 1(b) and Fig. 1(c), showing a cross-sectional side view along the direction of light propagation. Generally, light enters from the left and is mostly absorbed by the PD and then converted to photocurrents. The first scenario, Fig. 1(b), shows that buried SiO_2 is locally removed over a small area. Oxide is etched away, down to bare Si, and in this trench the GeSn virtual substrate is grown, which then is the foundation for the p-i-n PD. This is the in-line coupling or coaxial case in which the Si guided mode axis aligns exactly with the i-GeSn centerline. The second scenario, Fig 1(c), shows that the SOI top layer is not disturbed (except for local strip etching) and that the GeSn VS is grown first on that Si film, after which the p-i-n PD is deposited upon the VS. From the optical point-of-view, the incoming light from the first Si strip will be upwardly coupled into the GeSn regions because the GeSn constitutes a "leaky top cladding" for the Si since the GeSn has a refractive index (RI) higher than that of Si. This evanescent longitudinal-and-side coupling into GeSn gives the needed optical absorption.

3. Theoretical Models

In this section, we describe the theoretical models used to analyze the performance of the proposed GeSn WGPDs, including the carrier saturation velocities in GeSn material, the absorption coefficient, 3-dB BW, optical responsivity, R_0A parameters, and detectivity. Due to the limited availability of experimental data for GeSn alloys, the material parameters of GeSn alloys used in this study were obtained from a linear interpolation between these of Ge and α-Sn [37]. With the availability of more experimental data, it is expected that our calculations can predict the device's performance more accurately.

Preprints (www.preprints.org) | NOT PEER-REVIEWED | Posted: 29 April 2022 doi:10.20944/preprints202204.0294.v1

3.1. Absorption Coefficient

In $Ge_{1-x}Sn_x$, the photon absorption takes place due to (1) the direct bandgap interband transition from the valance band (VB) to the Γ-valley conduction band (CB), and (2) the indirect bandgap interband transition from the VB to the L-valley CB. The direct-band optical absorption coefficient (α_{dir}) of $Ge_{1-x}Sn_x$ alloys can be calculated using the Fermi's golden rule by taking into account the nonparabolicity effect and Lorentzian lineshape function as [13, 14],

$$\alpha_{dir}(\hbar\omega) = \frac{\pi\hbar e^2}{n_r c\varepsilon_0 m_0^2 \hbar\omega}\sum_m \int \frac{2d\mathbf{k}}{(2\pi)^3}\left|\hat{e}.p_{CV}\right|^2 \times \frac{\gamma/2\pi}{\left[E_{C\Gamma}(\mathbf{k}) - E_m(\mathbf{k}) - \hbar\omega\right]^2 + (\gamma/2)^2} \tag{1}$$

where n_r represents the RI of the active medium, c is the velocity of light in vacuum, ε_0 is the free space permittivity, m_0 is the electron's rest mass, ω is the angular frequency of incident light, e is the electronic charge, $\hbar$ is the reduced Planck's constant, $\left|\hat{e}\cdot p_{CV}\right|^2 = m_0 E_P/6$ indicates the momentum matrix, E_P denotes the optical energy, γ is the full-width-at-half-maximum (FWHM) of the Lorentzian lineshape function. $E_{C\Gamma}(\boldsymbol{k})$ and $E_m(\boldsymbol{k})$ represent the electron and hole energy in the Γ-valley CB and VB, respectively, with **k** being the wavevector, which are calculated using a multi-band k·p method [14, 37, 38]. The summations over m indicate all interband transitions from the VB, including the heavy hole (HH) and light hole (LH) bands, to the Γ-valley CB. On the other hand, the indirect-band optical absorption coefficient (α_{indir}) can be calculated using the following empirical expression [39],

$$\alpha_{\text{indir}} = A\left(\hbar\omega - E_g^L + E_{ap}\right)^2 + A\left(\hbar\omega - E_g^L - E_{ap}\right)^2 \tag{2}$$

where the first (second) term denotes the acoustic phonon absorption (emission) mechanism which occurs for $\hbar\omega > E_g^L - E_{ap}\left(\hbar\omega > E_g^L + E_{ap}\right)$, with E_g^L denoting the indirect bandgap energy and with E_{ap} being the energy of acoustic phonon. Due to the unavailability of GeSn related experimental data and the similarity of the band structures of GeSn and pure Ge, in this analysis the values for GeSn are approximated by these of pure Ge (A = 2717 cm^{-1} [13, 40] and E_{ap} = 27.7 meV at room temperature [41]). Thus, the total optical absorption coefficient (α) can be expressed as,

$$\alpha = \alpha_{\text{dir}} + \alpha_{\text{indir}} \tag{3}$$

The penetration depth (d) can then be calculated by,

$$d = \frac{1}{\alpha} \tag{4}$$

3.2. Saturation Velocity and Bandwidth

The BW of a PD is dominated by two mechanisms, transit-time delay and RC delay. The transit-time-delay limited BW (f_T) can be calculated using [25],

$$f_T = 0.45\frac{v_S}{t_i} \tag{5}$$

where t_i represents the thickness of the intrinsic $Ge_{1-x}Sn_x$ active region and v_S is the carrier saturation velocity. Previously, the carrier saturation velocity was usually approximated by that of Ge due the lack of experimental data of GeSn. However, it is well known that the carrier mobilities of GeSn significantly increase with increasing Sn content [13,15]. As a result, the carrier saturation velocity of GeSn should vary significantly compared to pure

Ge. Therefore, here we theoretically calculate the carrier mobilities of GeSn alloys. The carrier saturation velocity can be calculated by [42],

$$v_S = \sqrt{\frac{\Delta E}{m^* \sigma_s N_s L_{me}}} \tag{6}$$

where $\Delta E = hc_s / a_{\mathrm{GeSn}}$, h is the Planck's constant, c_s is the velocity of sound in the GeSn material which can be obtained by $c_s = \sqrt{\mu/\rho}$ with μ being the shear modulus and ρ being the density, a_{GeSn} is the lattice constant of GeSn, m^* is the conductivity effective mass which is taken from the calculation results using 30-band full-zone k·p method [43], N_s $\left(= 8/a_{GeSn}^3\right)$ is the atomic density of GeSn alloys, $L_{me} = N_s^{-1/3}$ is the mean free path [42], and σ_s is the capture cross-sectional area of the atom. Due to the lack of value of capture cross-sectional area of GeSn alloys, in this analysis we approximate the capture cross-sectional area using that of pure Ge atom i.e. σ_s=1×10^{-17} cm^{-2} [42]. The lattice constant of bulk $Ge_{1-x}Sn_x$ (a_{GeSn}) can be calculated by [44],

$$a_{\mathrm{GeSn}} = (1-x)a_{\mathrm{Ge}} + xa_{\mathrm{Sn}} + x(1-x)\theta_{\mathrm{GeSn}} \tag{7}$$

where a_{Ge} = 5.6573 Å and a_{Sn} = 6.4892 Å are the bulk lattice constants of Ge and Sn, respectively, and θ_{GeSn} = 0.041 Å is the bowing parameter [44]. The RC-delay limited BW (f_{RC}), on the other hand, can be calculated using [25],

$$f_{RC} = \frac{1}{2\pi RC} \tag{8}$$

where C is the capacitance of the intrinsic GeSn region, which can be calculated using $C = \varepsilon A_d / t_i$ with ε being the permittivity of the GeSn alloy, $A_d (= w \times L)$ is the cross-sectional area of the active region and R denotes the load resistance. In this analysis, the standardized RF impedance of R = 50 Ω has been considered [24,25]. Note that the parasitic capacitance of the device is not considered in this study. The parasitic capacitance of the device can increase the RC time delay, but it be minimized by optimizing the design of electrodes. Using Eqs. (5) and (8), the total 3-dB BW can be calculated as [25],

$$f_{3dB} = \sqrt{\frac{1}{f_T^{-2} + f_{RC}^{-2}}} \tag{9}$$

With the 3-dB bandwidth, the response time (τ_r) can be calculated using

$$\tau_r \cong \frac{0.35}{f_{3\mathrm{dB}}}. \tag{10}$$

3.3. Optical Responsivity

The responsivity (R_λ) of WGPDs can be calculated using [45],

$$R_\lambda = \kappa \frac{e\lambda\eta_i}{hc} \frac{\Gamma\alpha}{\Gamma\alpha + \alpha_i}(1-R_s)\{1-\exp[-(\Gamma\alpha+\alpha_i)L]\} \tag{11}$$

where κ is coupling efficiency, λ is the wavelength of the incident light wave, η_i represents the internal quantum efficiency of the WGPD, Γ denotes the optical confinement factor (OCF) of the intrinsic $Ge_{1-x}Sn_x$ region, α is the total absorption coefficient of the active region given in Eq. (3), α_i indicates the internal absorption loss in the waveguide which

does not contribute to photocurrents, and R_s is the reflectivity of the WGPD. For maximum response, we have assumed no coupling loss (κ = 1), perfect internal quantum efficiency (η_i =100%), and zero reflection (R_s = 0), with the understanding that any less-than-ideal conditions can be accounted for proportionally.

3.4. Dark Current

In this defect-free GeSn WGPD, the minority carriers' diffusion is the primary source of the dark current and the Shockley-Read-Hall (SRH) recombination process in the materials and at the GeSn sidewalls are not considered [46] as mentioned in Ref. [13]. Therefore, by considering the short-base diode approximation, the dark current density (J_{dark}) can be calculated using [13],

$$J_{dark} = J_{diff}^{\Gamma} + J_{diff}^{L} + J_{diff}^{h} = J_0 \times \left[\exp\left(\frac{eV}{k_B T} \right) - 1 \right] \tag{12}$$

where V is the applied bias, k_B is the Boltzmann constant, T is the temperature and J_0 indicates the reverse saturation current density which can be expressed in terms of diffusion of electrons in Γ- and L-valley and holes as [13],

$$J_0 = e\frac{D_n^{\Gamma}}{t_p} n_{p0}^{\Gamma} + e\frac{D_n^{L}}{t_p} n_{p0}^{L} + e\frac{D_p}{t_n} p_{n0} \tag{13}$$

where D_p, D_n^{Γ} and D_n^{L} represent the diffusion coefficients of holes and electrons in the Γ- and L-valley, respectively, p_{n0}, n_{p0}^{Γ} and n_{p0}^{L} denote the minority concentration of holes and electrons in Γ- and L-valley, respectively.

3.5. R_0A Product and Detectivity

The differential zero bias resistance (R_0) can be calculated by [47],

$$R_0 = \frac{k_B T}{e I_0} \tag{14}$$

where I_0 is the diode reverse current. From Eq. (13), we can define R_0A parameter in terms of the J_0 as,

$$R_0 A = \frac{k_B T}{e J_0} \tag{15}$$

The detectivity (D^*) of the GeSn WGPD can be expressed as [22, 38],

$$D^* = \frac{R_\lambda \sqrt{A_d \Delta f}}{\sqrt{\langle i_n^2 \rangle}} \tag{16}$$

where Δf denotes the BW. Under dark condition, the thermal noise can be evaluated by [13, 38],

$$\langle i_n^2 \rangle = \frac{4 k_B T \Delta f}{R_0} \tag{17}$$

Hence, using Eqs. (14)-(16) the detectivity of the GeSn WGPD can be written as,

Preprints (www.preprints.org) | NOT PEER-REVIEWED | Posted: 29 April 2022 doi:10.20944/preprints202204.0294.v1

$$D^* = \frac{R_\lambda}{2}\sqrt{\frac{R_0 A}{k_B T}} \tag{18}$$

4. Results and Discussions

In this section, we first investigate the absorption spectra, penetration depth and the OCF of the GeSn active layer and then calculate the carriers' saturation velocity of the holes and electrons in the Γ- and L-valleys to estimate the BW. After that, we optimize the different structural parameters of the proposed GeSn WGPD including the thickness of the intrinsic region (t_i), length of the photon absorbing layer (L), Sn concentration (x) of the GeSn active region to achieve the highest responsivity-bandwidth product (RBWP) at λ = 2 μm. Finally, we calculate the detectivity of the optimally designed GeSn WGPDs.

4.1. Absorption Coefficient

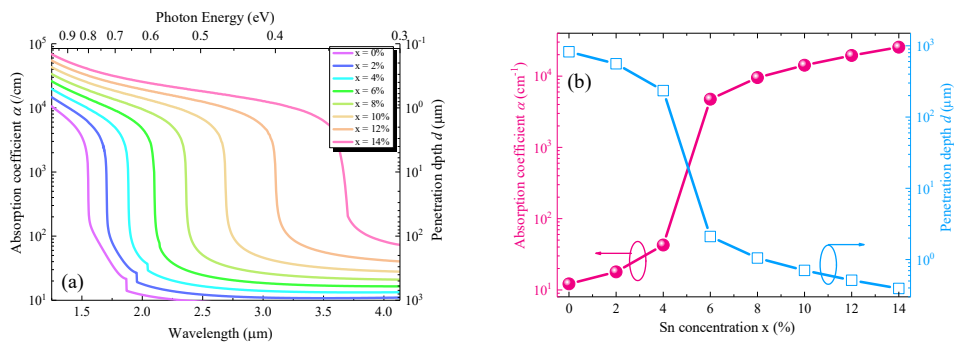

Figure. 2. (**a**) Calculated total absorption coefficient and penetration depth spectra of GeSn WGPD for different Sn concentrations. (**b**) Calculated total absorption coefficient and penetration depth with various Sn concentrations at λ = 2 μm.

Figure 2(a) shows the calculated total optical absorption coefficient and penetration depth spectra with different Sn concentrations. It can be noted that for a particular Sn concentration, the absorption coefficient decreases with increasing wavelength. As a result, the penetration depth also increases, suggesting that a longer device length is required for effective absorption in the WGPD. The increase of Sn concentration reduces the direct and indirect bandgaps of the GeSn alloys [13]. Therefore, the absorption edge shows a redshift, thereby extending the photodetection range towards longer wavelengths and reducing the penetration depth. Figure 2(b) shows calculated total absorption coefficient and penetration depth at λ = 2 μm with different Sn concentrations. The bandgap of the $Ge_{1-x}Sn_x$ alloy (x < 6%) is not small enough, leading to very small the absorption coefficient at λ = 2 μm. Thus, to obtain high absorption (> 10^3 cm^{-1}) at λ = 2 μm for efficient photodetection, the Sn concentration should be higher than 6%. On the other hand, for x < 6%, the penetration depth of > 100 μm proves that the GeSn WGPD with lower Sn concentration requires longer device length for sufficient absorption of the incident photons.

4.2. Optical Confinement Factor

Preprints (www.preprints.org) | NOT PEER-REVIEWED | Posted: 29 April 2022 doi:10.20944/preprints202204.0294.v1

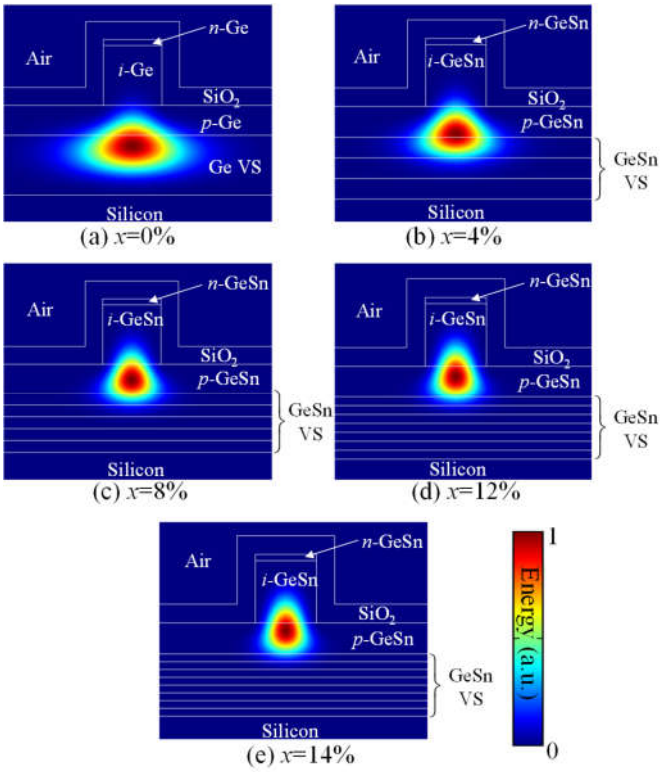

Figure. 3. Simulated energy distribution for the quasi transverse-electric fundamental mode of the GeSn WGPD for different Sn concentrations at $\lambda = 2$ μm.

To investigate the OCF of the GeSn WGPDs, we have obtained various modes by using the finite element method (FEM), where the RIs of the materials are taken from Refs. [23,40]. The simulated energy distributions of the quasi-transverse-electric fundamental (TE_{00}) mode at $\lambda = 2$ μm for different Sn concentrations with $t_i = 1000$ nm are illustrated in Fig. 3 (for TE_{00} mode, the dominant fields are E_x and H_y). For $x = 0\%$, there is no difference in RI between the *p-i-n* structure and the VS. As a result, the optical confinement is provided by the lower-RI bulk Si substrate ($n = 3.45$) and the top SiO_2 layer ($n = 1.45$). As a result, light cannot be properly confined in the *i*-Ge active layer, but leak to the Ge VS and *p*-Ge layer, yielding a small OCF of 2.67% for the active layer. As the Sn concentration increases, the RI of the *i*-$Ge_{1-x}Sn_x$ active layer increases, thereby pushing up the optical field, and enhancing the optical confinement inside the *i*-$Ge_{1-x}Sn_x$ active layer. Figure 4 shows the calculated OCF for fundamental TE_{00} mode for the *i*-$Ge_{1-x}Sn_x$ active layer as a function of Sn concentration as well as the thickness of the active region at $\lambda = 2$ μm. The increase of active layer thickness can significantly enhance the OCF because the *i*-$Ge_{1-x}Sn_x$ active layer occupies a larger portion of the waveguide. On the other hand, increasing the Sn composition can also increase the OCF for the GeSn active layer due to the increased RI difference between the GeSn active layer and the VS.

Preprints (www.preprints.org) | NOT PEER-REVIEWED | Posted: 29 April 2022 doi:10.20944/preprints202204.0294.v1

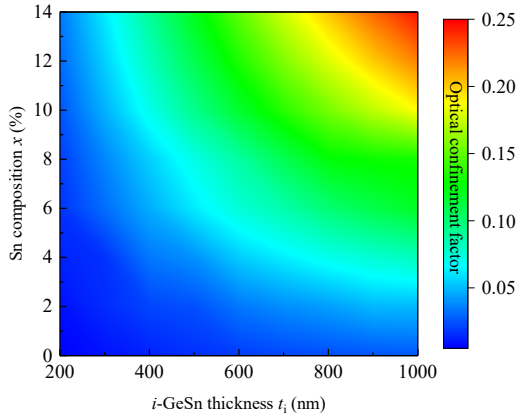

Figure. 4. Simulated optical confinement factor for the quasi transverse-electric fundamental mode for the GeSn active layer as a function of thickness and Sn concentration of the GeSn WGPD at $\lambda = 2$ μm.

4.3. Carrier Saturation Velocity

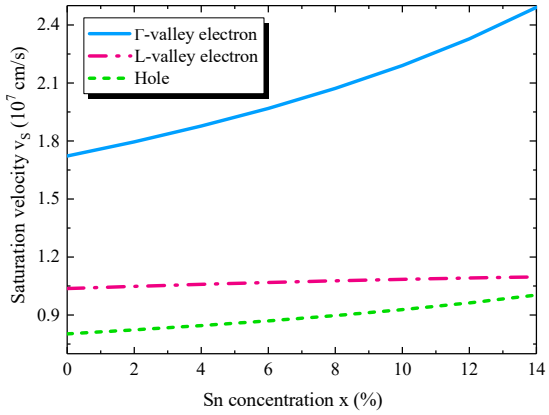

Figure. 5. Calculated carrier saturation velocity as a function of Sn concentration inside the active region.

Here we theoretically analyze the saturation velocity of the holes and electrons in the Γ- and L-valleys of GeSn using Eq. (6). Figure 5 shows the calculated saturation velocities as a function of Sn concentration. The increase of Sn concentration reduces the effective masses of the carriers, and thus enhances the carrier mobilities [13]. As a result, the saturation velocities increase with the increase of Sn concentration. The analysis suggests that carriers take less time to transit through the active layer, thereby beneficial for increasing the transit-time-delay limited BW. For the saturation velocity of electrons, as the electrons in Γ-valley CB have much smaller effective mass than that of L-valley electrons [13, 43], they have much higher saturation velocity than these in the L-valley CB. On the other hand, the hole saturation velocity is much smaller than the electron saturation velocities due to the larger effective mass. Therefore, the holes take longer time to transit through the $Ge_{1-x}Sn_x$ active region than the electrons. As a result, the holes' movement entirely dominates the transit-time-delay limited BW of the GeSn WGPDs.

4.4. Bandwidth

Preprints (www.preprints.org) | NOT PEER-REVIEWED | Posted: 29 April 2022 doi:10.20944/preprints202204.0294.v1

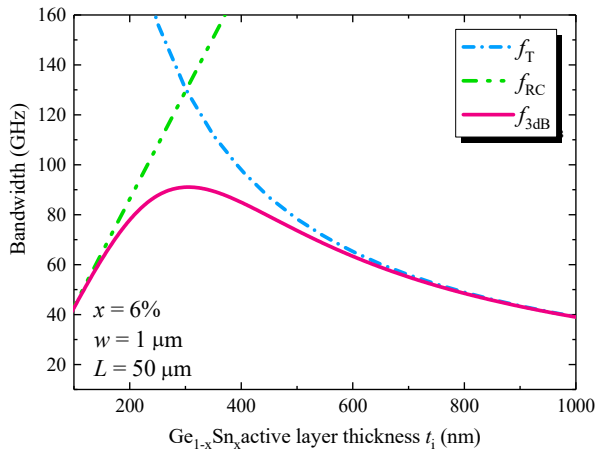

Figure. 6. Calculated transit-time-delay limited BW, RC-delay limited BW and 3-dB BW as a function of $Ge_{1-x}Sn_x$ active layer thickness.

Next, we calculate the transit-time-delay BW, RC-delay BW and 3-dB BW for the $Ge_{1-x}Sn_x$ WGPDs using Eqs. (5), (8) and (9). For the transit-time-delay, we consider hole time delay as it is significantly larger than the electron time delay as discussed in Section 4 (*4.3*). Figure 6 shows the transit-time limited BW, RC limited BW and 3-dB BW as a function of the GeSn active region thickness with x = 6% and a device length of L = 50 μm. When the thickness of active region increases, the holes require longer time to transit through the entire region, leading to decreased transit-time-delay limited BW. On the other hand, the capacitance of the intrinsic $Ge_{1-x}Sn_x$ active layer reduces with increased GeSn active thickness, so the RC-delay limited BW increases. Therefore, the total 3-dB BW first increases with the increase of intrinsic $Ge_{1-x}Sn_x$ thickness, reaches a peak value, and then decreases for further increase of its thickness. The peak 3-dB BW of ~91 GHz can be achieved for 300 nm thick $Ge_{1-x}Sn_x$ active layer. Similar results have been obtained for other Sn concentrations and other lengths.

4.5. Optimization of the GeSn WGPD at 2 μm

In this section, we optimize different structural parameters of our proposed GeSn WGPD to achieve high-BW and high responsivity simultaneously at λ = 2 μm. First, we depict the responsivity and 3-dB BW as a function of thickness of the $Ge_{1-x}Sn_x$ active region in Fig. 7(a) to obtain the optimum thickness of the $Ge_{1-x}Sn_x$ active region. The responsivity increases with increase of GeSn active layer thickness due to the increased OCF. For t_i > 800 nm, the responsivity exhibits a saturation trend. On the other hand, the 3-dB BW first increases with increased thickness of the GeSn active layer, reaches a peak value of 91 GHz at t_i = 400 nm, and then decreases with further increase of thickness. Between t_i = 300-600 nm, the BW achieves more than 60 GHz with responsivity of R_λ > 0.8 A/W. For optimal thickness, we have calculated RBWP using Eqs. (9) and (10) and plotted as a function of $Ge_{1-x}Sn_x$ active region thickness in Fig. 7(b). The RBWP shows a peak value at t_i = 400 nm (marked by the red arrow), which is considered as the optimal thickness of the $Ge_{1-x}Sn_x$ active layer to achieve high-BW and high responsivity simultaneously at λ = 2 μm.

Preprints (www.preprints.org) | NOT PEER-REVIEWED | Posted: 29 April 2022 doi:10.20944/preprints202204.0294.v1

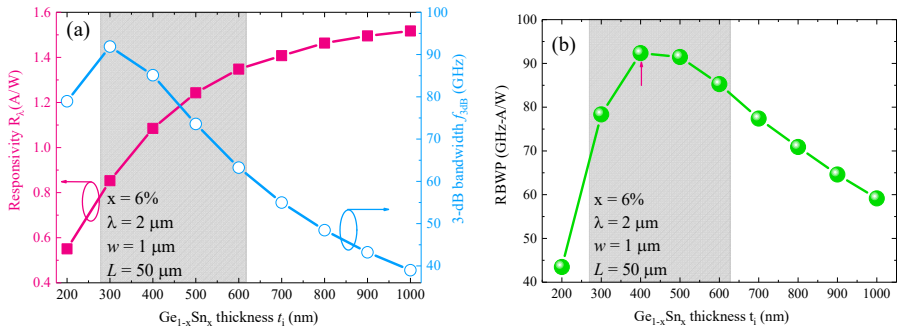

Figure. 7. (**a**) Calculated responsivity and 3-dB bandwidth as a function of $Ge_{1-x}Sn_x$ active layer thickness at λ = 2 μm. (**b**) Calculated responsivity-bandwidth product (RBWP) against $Ge_{1-x}Sn_x$ thickness at λ = 2 μm.

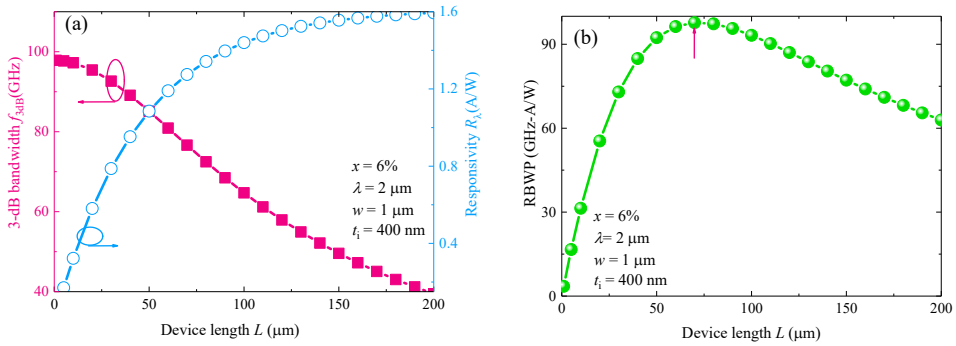

Figure. 8. (**a**) Calculated 3dB bandiwdth and responsivity as a function of device length at λ = 2 μm. (**b**) Calculated responsivity-bandwidth product (RBWP) as a function of device length at λ = 2 μm.

After obtaining the optimal thickness of the GeSn active layer, next we investigate the optimal device length (L_0) to obtain highest performance at λ = 2 μm. Figure 8(a) depicts the variation of the responsivity as well as the total 3-dB BW with the device length (x = 6%). It can be noted that for 1 μm device length, our proposed GeSn WGPD can yield a high BW of ~98 GHz, but the corresponding responsivity is only ~0.036 A/W. Increase of device length increases the effective area and thereby the capacitance, so RC-delay limited BW reduces as well as the total 3-dB BW. In addition, the responsivity increases with the increase of device length due to the longer photon-absorbing path. In order to obtain the optimal device length to achieve high-BW and high responsivity simultaneously at λ = 2 μm, we therefore evaluate RBWP as a function of device length as shown in Fig. 8(b). The peak RBWP occurs at L = 70 μm (marked by the red arrow), corresponding to a BW of ~77 GHz and a responsivity of 1.275 A/W. Thus, L = 70 μm is considered as the optimal length of the device. For other Sn compositions, the optimal device length to achieve highest RBWP is also obtained using the same procedures. Figure 9(a) shows the variation of optimum length of the GeSn WGPD with different Sn concentrations at λ = 2 μm. For pure Ge, to achieve highest RBWP at 2 μm wavelength, a very long device length of L_0 = 1130

Preprints (www.preprints.org) | NOT PEER-REVIEWED | Posted: 29 April 2022 doi:10.20944/preprints202204.0294.v1

μm is needed due to the negligible absorption coefficient. With the incorporation of Sn, the optimal length decreases with the Sn concentration x due to the enhanced absorption coefficient and reduced penetration depth of the GeSn active layer. For $x > 6\%$, the optimal length decreases to only $L_0 < 70$ μm. The small device length also indicates a small device footprint for high density EPICs. With the optimal length of the device, we then calculate the responsivity and 3-dB bandwidth of the optimized GeSn WGPDs, and the results are depicted in Fig. 9(b). For $x < 6\%$, both the responsivity and 3-dB BW are small due to the small absorption coefficient. For the Sn composition ranging from 6% to 14%, the responsivity and 3-dB bandwidth can be significantly enhanced to achieve high-performance photodetection at λ = 2 μm. In addition, the responsivity does not significantly change for $6\% < x < 14\%$. Therefore, we have considered $x = 10\%$ with $L_0 = 32$ μm as the optimal length of the GeSn WGPD.

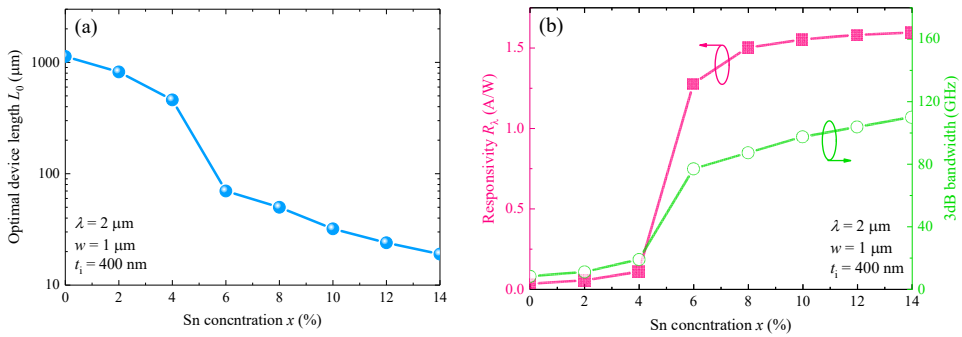

Figure. 9. (**a**) Variation of optimum length of the GeSn waveguide photodetectors with various Sn concentrations at λ = 2 μm. (**b**) Variation of 3-dB bandwidth and responsivity against Sn concentration for optimized GeSn waveguide photodetectors.

4.6. Responsivity

Based on the optimized geometrical structure (t_i = 400 nm and L_0 = 32 μm) of our proposed GeSn WGPD, we calculate the responsivity spectra with different Sn concentrations, and the results are shown in Fig. 10. The increase of Sn concentration increases the responsivity and extends the photodetection capacity towards longer wavelength. For $x < 6\%$, the $Ge_{1-x}Sn_x$ alloy cannot effectively absorb the photons at λ = 2 μm due to its higher bandgap, leading to negligible responsivity. With $x > 6\%$, the direct bandgap has been significantly reduced, thereby enabling efficient photodetection at λ = 2 μm. For $x > 8\%$, the photodetection range can fully cover the entire 2 μm wavelength band.

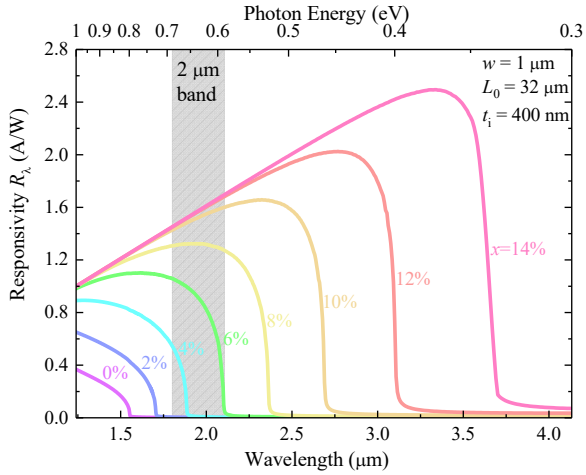

Figure. 10. Calculated responsivity spectra of GeSn waveguide photodetectors for different Sn concentrations.

4.7. Dark Current and R_0A parameter

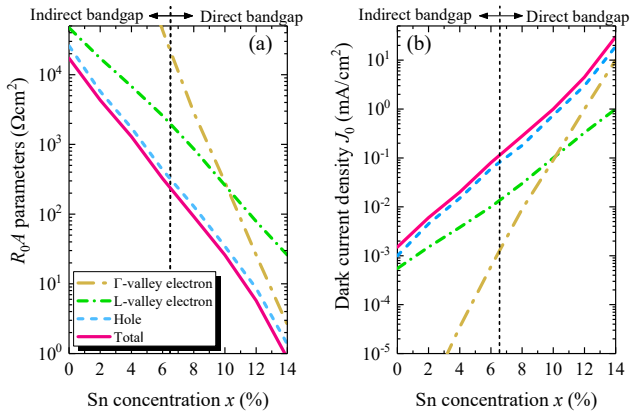

Figure. 11. (**a**) Variation of different components and total R_0A parameters and (**b**) dark current densities of GeSn WGPD with Sn concentration.

Eqs. (12) and (15), we calculate the dark current density (J_{dark}) under zero-bias condition and the R_0A parameter of the GeSn WGPD as a function of Sn composition. Figure 11(a) illustrates the calculated R_0A induced by different components and the total R_0A parameter as well as the dark current density as a function of Sn concentration. The increase of Sn concentration reduces the bandgap, thereby increasing the intrinsic carrier concentration, then the diffusion currents [13]. Therefore, all the R_0A components and the total R_0A parameters decrease with increase of Sn concentration. As $t_n \ll t_p$, the hole R_0A components are dominant over the electron components. When the Sn concentration is lower than 6.6%, the $Ge_{1-x}Sn_x$ alloys are an indirect bandgap material [13], thus injected minority electrons populate the L-valley more rather than the Γ-valley. Therefore, the R_0A for L-valley electrons is lower than that of Γ-valley electrons. However, when the Sn concentration exceeds 6.6%, the Γ-valley CB is lower than the L-valley CB, so more electrons can populate Γ-valley CB. As a result, the R_0A parameter of the Γ-valley electrons reduces rapidly. In that condition, the contribution of Γ-valley electrons is dominant over those of L-valley electrons.

Preprints (www.preprints.org) | NOT PEER-REVIEWED | Posted: 29 April 2022 doi:10.20944/preprints202204.0294.v1

4.8. Detectivity

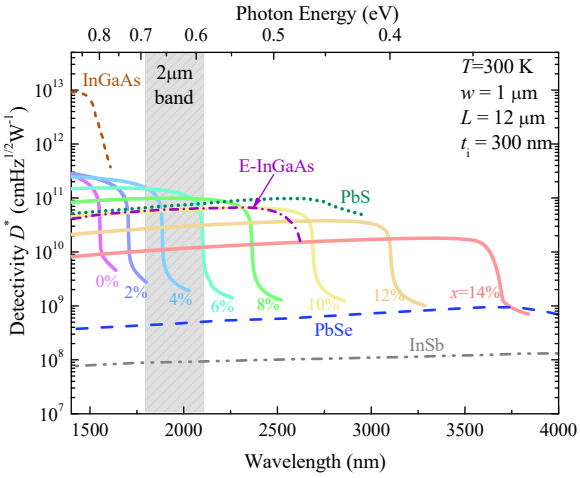

Figure. 12. Calculated detectivity spectra of GeSn waveguide photodetectors with different Sn concentrations compared with selected SWIR and MIR PDs.

With the responsivity of the optimally designed GeSn WGPD and R_0A at T = 300 K, we then further calculate the detectivity spectra for the GeSn WGPD with different Sn concentrations (Fig. 12) compared with those of selected SWIR and MIR PDs. For a fixed Sn composition, the detectivity value decreases with increasing wavelength, and become negligible at the direct-gap absorption edge (the direct bandgap energy). The tunability of bandgap due to the incorporation of Sn helps cover different spectral range according to the applications of interest. With an increase of Sn content, the cutoff wavelength of detectivity redshifts, but the magnitude of detectivity also decreases. In comparison with the commercially available uncooled (T = 300 K) SWIR and MIR PDs [13], it is found that although InGaAs PDs have highest detectivity, the cutoff wavelength is only 1.7 μm, which hinders the applications for 2 μm wavelength band detection. The GeSn PDs with x = 8% can achieve photodetection range fully covering the entire 2 μm wavelength band with a detectivity of > 9.48×10^{10} $cmHz^{½}W^{-1}$. In addition, the GeSn PDs with x = 10% can have performance superior than E-InGaAs PDs, and comparable to PbS PDs. It is also noted that the detectivity of GeSn WGPDs are also much higher than PbSe and InSb PDs. Thus, we can conclude that our proposed GeSn WGPD can be a strong competitor of these commercial devices.

MIR and SWIR PDs are usually operated at cryogenic temperatures. If the operating temperature of the GeSn WGPDs is lowered, there are several impacts. First, the bandgap energy of GeSn becomes larger [48], so the direct-gap absorption edge will blue shift, resulting in a reduced photodetection range. Second, the intrinsic carrier density will decrease, thereby significantly suppressing the dark current. As a result, the detectivity of the GeSn WGPDs will be significantly enhanced.

Preprints (www.preprints.org) | NOT PEER-REVIEWED | Posted: 29 April 2022 doi:10.20944/preprints202204.0294.v1

4.9. Optimum structures and optimum performances of the GeSn WGPDs

In this section we present the optimum structure as well as optimum performances of the GeSn WGPDs for different Sn concentration (6%-14%). This comparative study is shown in the table 1.

Table 1. Comparative Study of the Optimally Designed GeSn WGPD for different Sn concentration at 2 μm Wavelength

Sn Content x (%)	Optimum Length L_0 (μm)	Optimum Performance			
		Responsivity R_λ (A/W)	Bandwidth f_{3dB} (GHz)	Response time τ_r(ps)	Detectivity D^* (cmHz$^{1/2}$W^{-1})
06	70	1.275	77	4.54	1.78×10^{11}
08	50	1.499	128	2.73	1.12×10^{11}
10	32	1.549	87	4.02	6.29×10^{10}
12	24	1.578	103	3.39	2.94×10^{10}
14	19	1.594	110	3.18	1.15×10^{10}

4.10. Comparative Study of different GeSn PDs

Table 2 contains a comparative study of the responsivity obtained from our optimally designed GeSn WGPD with previously reported different GeSn PDs at 2 μm. This proposed GeSn WGPD can achieve better performance than previously reported PDs.

Table 2. Comparative Study of the Optimally Designed GeSn WGPD with previously reported GeSn PDs at T = 300 K

Sn Concentration (%)	Substrate	Active layer Thickness (nm)	Responsivity (A/W)	Reference
4.7	SOI	390	0.065	[49]
10	SOI	370	1.02	[24]
10	Si	270	1.51	[25]
4.3	Si	400	0.06	[36]
10	Si	3000	1.59	[13]
4.2	SOI	540	0.0022	[50]
10	Si	400	1.55	This work

5. Conclusions

In conclusion, we have designed and optimized a new type of homojunction waveguide-coupled GeSn PD to achieve an optimum performance at 2 μm wavelength in the Si- or SOI-wafer EPIC platform. First, we theoretically calculate the carrier saturation velocities of the GeSn alloy. The incorporation of Sn reduces the effective mass of the carriers and thus the saturation velocity increases above that of pure Ge, suggesting that the GeSn-based devices have higher operational speed than the pure-Ge-based devices. By carefully designing the length of the photodetection layer, the thickness of the photo-generated

carrier collection path and Sn concentration, our proposed GeSn WGPD with 10% Sn concentration can give responsivity of 1.549 A/W with ~97 GHz BW and detectivity of 6.12×10^{10} $cmHz^{½}W^{-1}$ at room temperature. The compatibility with standard Si based CMOS technology; monolithically integrability on same Si chip; high operational speed as well as high responsivity and detectivity make this proposed device an effective candidate for state-of-the-art silicon photonics for high-speed communication applications at 2 μm wavelength band.

Author Contributions: "Conceptualization, G.E.C; methodology, S.G, G.S., and G.E.C.; software, S.G., R.B., and G.E.C.; validation, S.G., R. B., G.E.C. G.S., R.S., and H.H.C. formal analysis, data curation, S.G., R. B., G.E.C. G.S., R.S., and H.H.C; writing—original draft preparation, S.G.; writing—review and editing, S.G., R. B., G.E.C. G.S., R.S., and H.H.C; supervision, G.E.C.; project administration, G.E.C..; funding acquisition, G.E.C.

Funding: This work was supported in part by the Young Scholar Fellowship Program by Ministry of Science and Technology (MOST) Taiwan, under the grant number MOST 110-2636-E-194-002, and in part by Air Force Office of Scientific Research under the under grant numbers FA9550-19-1-0341 and FA9550-21-1-0347.

Acknowledgments: The authors would like to thank the Advanced Institute of Manufacturing with High-tech Innovations (AIM-HI) from The Featured Areas Research Center Program within the framework of the Higher Education Sprout Project by the Ministry of Education (MOE) in Taiwan.

Conflicts of Interest: The authors declare no conflict of interest.

References

1. Ellis, A. D.; Zhao, J.; Cottar, D. Approaching the non-linear Shanon limit. *J. Lightwave Technol.* **2010**, 28, 423-433.
2. Roberts, P. et. al. Ultimate low loss of hollow-core photonic crystal fibers. *Opt. Express* **2005**, 13, 236-244.
3. Li, Z.; Heidt, A.M.; Simakov, N.; Jung, Y.; Daniel, J. M. O.; Alam, S. U.; Richardson, D. J. Diode-pumped wideband thulium-doped fiber amplifiers for optical communications in the 1800-2050 nm window. *Opt. Express* **2013**, 21, 26450-26455.
4. Gunning, F.; Corbett, B. Time to Open the 2-μm Window? *Optics and Photonics News* **2019**, 42-47.
5. Chen, Y.; Zhao, X.; Huang, J.; Deng, Z.; Cao, C.; Gong, Q.; Chen, B. Dynamic model and bandwidth characterization of InGaAs/GaAsSb type-II quantum wells PIN photodiodes. *Opt. Express* **2018**, 26, 35034-35045.
6. Chen, Y.; Xie, Z.; Huang, J.; Deng, Z.; Chen, B. High-speed uni-traveling carrier photodiode for 2 μm wavelength application. *Optica* **2019**, 6, 884-889.
7. Soref, R. Silicon-based Silicon-germanium-tin Heterostructure Photonics. *Philos. Trans. R. Soc. A.* **2014**, *372*, 20130113.
8. Deen, M. J.; Basu, P. K. Silicon Photonics: Fundamentals and Devices; Willey: Hoboken, NJ, USA, 2012.
9. Michel, J.; Liu, J.; Kimerlin, L. C. High-performance Ge-on-Si Photodetectors. *Nat. Photonics* **2010**, 4, 527–534.
10. Gupta, J. P.; Bhargava, N.; Kim, S.; Adam, T.; Kolodzey, J. Infrared Electroluminescence from GeSn Heterojunction Diodes Grown by Molecular Beam Epitaxy. *Appl. Phys. Lett.* **2013**, 102, 251117.
11. Yu, I. S.; Wu, T. H.; Wu, K. Y.; Cheng, H. H.; Mashanov, V.; Nikiforov, A.; Pchelyakov, O.; Wu, X. S. Investigation of $Ge_{1-x}Sn_x$/Ge with high Sn composition grown at low-temperature. *AIP Advances* **2011**, 1, 042118.
12. Ghetmiri, S. A.; Du, W.; Margetis, J.; Mosleh, A.; Cousar, L.; Conley, B. R.; Domulevicz, L.; Nazzal, A.; Sun, G.; Soref, R. A.; Tolle, J.; Li, B.; Naseem, H. A.; Yu, S. Q. Direct-bandgap GeSn grown on silicon with 2230 nm photoluminescence. *Appl. Phys. Lett.* **2014**, 105, 151109.
13. Chang, G. -E.; Yu, S. -Q.; Liu, J.; Cheng, H. H.; Soref, R. A.; Sun, G. Achievable performance of uncooled homojunction GeSn mid-infrared photodetectors. *IEEE J. Sel. Quantum Electron.* **2022**, 28, 3800611.
14. Chang, G.E.; Basu, R.; Mukhopadhyay, B.; Basu, P.K. Design and Modeling of GeSn-based Heterojucntion Phototransistors for Communication Applications. *IEEE J. Sel. Quantum Electron.* **2016**, 22, 8200409.
15. Mukhopadhyay, B.; Sen, G.; Basu, R.; Mukhopadhyay, S.; Basu, P. K. Prediction of Large Enhancement of Electron Mobility in Direct Gap $Ge_{1-x}Sn_x$ Alloy. *Phys. Stat. Solidi B* **2017**, 254, 1700244.
16. Ghosh, S.; Mukhopadhyay, B.; Sen, G.; Basu, P.K. Study of Si-Ge-Sn based Heterobipolar Phototransistor (HPT) Exploiting Quantum Confined Stark Effect and Franz Keldysh Effect With and Without Resonant Cavity. *Phys. E* **2019**, 106, 62–67.
17. Ghosh, S.; Mukhopadhyay, B.; Sen, G.; Basu, P. K. Analysis of Some Important Parameters of Si-Ge-Sn RCE-HPT Exploiting QCSE and FKE. In Proceedings of the URSI-RCRS, Varanasi, India, 12–14 February 2020.
18. Ghosh, S. Comparative Study of Si-Ge-Sn Resonant Cavity Enhanced Heterojunction Bipolar Phototransistor under Quantum Confined Stark Effect and Franz Keldysh Effect at 1.55 μm. *IOSR J. Elec. Comm. Engg.* **2022**, 17, 1-10.
19. Hung, W. -T.; Barshilia, D.; Basu, R.; Cheng, H. H.; Chang, G. -E. Silicon-based High-responsivity GeSn Short-wave Infrared Heterojunction Phototransistors with a Floating Base. *Opt. Lett.* **2020**, 45, 1088–1091.

20. Kumar, H.; Basu, R.; Chang, G. -E. Impact of Temperature and Doping on the Performance of Ge/$Ge_{1-x}Sn_x$/Ge Heterojunction Phototransistors. *IEEE Photonics J.* **2020**, 12, 6801814.
21. Ghosh, S.; Mukhopadhyay, B.; Sen, G.; Basu, P. K. Performance analysis of GeSn/SiGeSn Quantum Well Infrared Photodetector in Terahertz Wavelength Region. *Phys. E* **2020**, 115, 113692.
22. Ghosh, S.; Bhattacharyya, A.; Sen, G.; Mukhopadhyay, B. Optimization of different structural parameters of GeSn/SiGeSn Quantum Well Infrared Photodetectors (QWIPs) for low dark current and high responsivity. *J. Comp. Electron.*, **2021**, 20, 1224-1233.
23. Tran, H.; Du, W.; Ghetmiri, S. A.; Mosleh, A.; Sun, G.; Soref, R. A. Margetis, J.; Tolle, J.; Li, B.; Naseem, H. A.; Yu, S. -Q. Systematic study of $Ge_{1-x}Sn_x$ absorption coefficient and refractive index for the device applications of Si-based optoelectronics. *J. Appl. Phys.* **2016**, 119, 103106.
24. Ghosh, S.; Mukhopadhyay, B.; Chang, G. -E. Design and Analysis of GeSn-Based Resonant-Cavity-Enhanced Photodetectors for Optical Communication Applications. *IEEE Sens. J.* **2020**, 20, 7801–7809.
25. Ghosh, S.; Kumar, H.; Mukhopadhyay, B.; Chang, G. -E. Design and modeling of high-performance DBR-based resonant-cavity-enhanced GeSn photodetector for fiber-optic telecommunication networks. *IEEE Sensors J.* **2021**, 21, 9900-9908.
26. Oehme, M.; Schmid, M.; Kaschel, M.; Gollhofer, M.; Widmann, D.; Kasper, E.; Schulze, J. GeSn p-i-n detectors integrated on Si with up to 4% Sn. *Appl. Phys. Lett.* **2012**, 101, 141110.
27. Tseng, H. H.; Li, H.; Mashanov, V.; Yang, Y. J.; Cheng, H. H.; Chang, G. -E.; Soref, R. A.; Sun, G. GeSn-based p-i-n Photodiodes with Strained Active Layer on a Si wafer. *Appl. Phys. Lett.* **2013**, 103, 231907.
28. Su, S.; Cheng, B.; Xue, C.; Wang, W.; Cao, Q.; Xue, H.; Hu, W.; Zhang, G.; Zuo, Y.; Wang, Q. GeSn p-i-n photodetector for all telecommunication bands detection. *Opt. Exp.* **2011**, 19, 6400.
29. Ghosh, S.; Lin, K. –C.; Tsai, C. –H.; Kumar, H.; Chen, Q.; Zhang, L.; Son, B.; Tan, C. S.; Kim, M.; Mukhopadhyay, B.; Chang, G. –E. Metal-Semiconductor-Metal GeSn Photodetectors on Silicon for Short-Wave Infrared Applications. *Micromachines* **2020**, 11, 795.
30. Tran, H.; Pham, T.; Du, W.; Zhang, Y.; Grant, P.; Grant, J.; Sun, G.; Soref, R.; Margetis, J.; Tolle, J.; Li, B.; Mortazavi, M.; Yu, S. Q. High performance $Ge_{0.89}Sn_{0.11}$ photodiodes for low-cost shortwave infrared imaging. *J. Appl. Phys.* **2018**, 124, 013101.
31. Xu, S.; Huang, Y. C.; Lee, K. H.; Wang, W.; Dong, Y.; Lei, D.; Panah, S.; Tan, C. S.; Gong, X.; Yeo, Y. C. GeSn lateral p-i-n photodetector on insulating substrate. *Opt. Express* **2018**, 26, 17312-17321.
32. Tran, H.; Pham, T.; Margetis, J.; Zhou, Y.; Dou, W.; Grant, P. C.; Grant, J. M.; Alkabi, S.; Du, W.; Sun, G.; Soref, R. A.; Tolle, J.; Li, B.; Mortazavi, M.; Yu, S. Study of high performance GeSn photodetectors with cutoff wavelength up to 3.7 μm for low-cost infrared imaging. CLEO: Science and Innovations 2019, San Jose, California United States, 5–10 May 2019.
33. Peng,Y.-H.; Cheng, H. H.; Mashanov, V. I.; Chang, G. -E. GeSn p-i-n waveguide photodetectors on silicon substrates. *Appl. Phys. Lett.* **2014**, 105, 231109.
34. Wang, H.; Zhang, J.; Zhang, G.; Chen, Y.; Huang, Y. C.; Gong, X. High-speed and high-responsivity p-i-n waveguide photodetector at a 2 μm wavelength with a $Ge_{0.92}Sn_{0.08}$/Ge multiple-quantum-well active layer. *Opt. Lett.* **2021**, 46, 2099-2102.
35. Huang, Y. -H.; Chang, G. -E.; Li, H.; Cheng, H. H. Sn-based waveguide p-i-n photodetector with strained GeSn/Ge multiple-quantum-well active layer. *Opt. Lett.* **2017**, 42, 1652.
36. Tsai, C. -H.; Lin, K. -C.; Cheng, C. -Y.; Lee, K. -C.; Cheng, H. H.; Chang, G. -E. GeSn lateral p-i-n waveguide photodetectors for mid-infrared integrated photonics. *Opt. Lett.* **2021**, 46, 864-867.
37. Chang, G. -E.; Chang, S. -W.; Chuang, S. L. Strain-Balanced Ge_zSn_{1-z}-$Si_xGe_ySn_{1-x-y}$ Multiple-Quantum-Well Lasers. *IEEE J. Quantum Electron.* **2010**, 46, 1813–1820.
38. Chuang, S.L. Physics of Photonic Devices, 2nd ed.; Willey: Hoboken, NJ, USA, 2012.
39. Pankove, J. I. Optical Processes in Semiconductors, Dover Publications, New York, USA, 1971.
40. Palik, E. D. Handbook of Optical Constants of Solids, Academic, Orlando, Florida, USA, 1985.
41. Schaevitz, R. K.; Ly-Gagnon, D. S.; Roth, J. E.; Edwards, E. H.; Miller, D. A. B. Indirect absorption in germanium quantum wells," *AIP Adv.* **2011**, 1, 032164.
42. Takata, I. A simple new model for the saturation velocity and the voltage dependency of leakage current. Proc. 9th International Symposium on Power Semiconductor Devices and IC's, Weimar, Germany, 26-29 May 1997.
43. Song, Z.; Fan, W.; Tan, C. S.; Wang, Q.; Nam, D.; Sun, G. Band structure of $Ge_{1-x}Sn_x$ alloy: a full-zone 30-band *k·p* model. *New J. Phys.* **2019**, 21, 073037.
44. Gencarelli, F. et. al. Crystalline properties and strain relaxation mechanism of CVD grown GeSn. *ECS J. Solid State Science and Technol.* **2013**, 2, P134-P137.
45. Fidaner, O.; Okyay, A. K.; Roth, J. E.; Schaevitz, R. K.; Kuo, Y. -H.; Saraswat, K. C.; Harris, J.S.; Miller, D. A. B. Ge–SiGe quantum-well waveguide photodetectors on silicon for the near-infrared. *IEEE Photon. Technol. Lett.* **2007**, 19, 1631-1633.
46. Chen, H. et. al. Dark current analysis in high-speed germanium *p-i-n* waveguide photodetectors. *J. Appl. Phys.* **2016**, 119, 213105.
47. Shi, X.; Phan, Q.; Weng, B.; McDowell, L. L.; Qiu, J.; Cai, Z.; Shi, Z. Study on the theoretical limitation of the mid-infrared PbSe N^+-P junction detectors at high operating temperature. *Detection* **2018**, 6, 1-16.

Preprints (www.preprints.org) | NOT PEER-REVIEWED | Posted: 29 April 2022 doi:10.20944/preprints202204.0294.v1

48. Lin, K. C.; Huang, P. R.; Li, H.; Cheng, H. H.; Chang, G. -E. Temperature-dependent characteristics of GeSn/Ge multiple-quantum-well photoconductors on silicon. *Opt. Lett.* **2021**, 46, 3604-3607.
49. Tsai, C. -H.; Huang, B. -J.; Soref, R. A.; Sun, G.; Cheng, H. H.; Chang, G. -E. GeSn resonant-cavity-enhanced photodetectors for efficient photodetection at the 2 μm wavelength band. *Opt. Lett.*, **2020**, 45, 1463-1466.
50. Chang, C. -Y.; Bansal, R.; Lee, K. -C.; Sun, G.; Soref, R.; Cheng, H. H.; Chang, G. -E. Planar GeSn lateral p-i-n resonant-cavity-enhanced photodetectors for short-wave infrared integrated photonics. *Opt. Lett.* **2021**, 46, 3316-3319.